



Examination of Sentinel-2A multi-spectral instrument (MSI) reflectance anisotropy and the suitability of a general method to normalize MSI reflectance to nadir BRDF adjusted reflectance



David P. Roy ^{*}, Jian Li, Hankui K. Zhang, Lin Yan, Haiyan Huang, Zhongbin Li

Geospatial Sciences Center of Excellence, 1021 Medary Ave, Wecota Hall, Box 506B, South Dakota State University, Brookings, SD 57007, USA

ARTICLE INFO

Article history:

Received 20 January 2017

Received in revised form 2 May 2017

Accepted 24 June 2017

Available online xxxx

Keywords:

Bidirectional reflectance distribution function (BRDF)

Sentinel-2

NBAR

MODIS

Landsat

Africa

ABSTRACT

The Sentinel-2A multi-spectral instrument (MSI) acquires multi-spectral reflective wavelength observations with directional effects due to surface reflectance anisotropy and changes in the solar and viewing geometry. Directional effects were examined by considering two ten day periods of Sentinel-2A data acquired close to the solar principal and orthogonal planes over approximately $20^\circ \times 10^\circ$ of southern Africa. More than 6.6 million (January 2016) and 10.6 million (April 2016) pairs of reflectance observations sensed 3 or 7 days apart in the forward and backscatter directions in overlapping Sentinel-2A orbit swaths were considered. The Sentinel-2A data were projected into the MODIS sinusoidal projection but first had to be registered due to a misregistration issue evident in the overlapping orbits. The top of atmosphere reflectance data were corrected to surface reflectance using the SEN2COR atmospheric correction software. Only pairs of forward and backward reflectance values that were cloud and snow-free, unsaturated, and had no significant change in their 3 or 7 day separation, were considered. The maximum observed Sentinel-2A view zenith angle was 11.93° . Greater BRDF effects were apparent in the January data (acquired close to the solar principal plane) than the April data (acquired close to the orthogonal plane) and at higher view zenith angle. For the January data the average difference between the surface reflectance in the forward and backward scatter directions at the Sentinel-2A scan edges increased with wavelength from 0.035 (blue), 0.047 (green), 0.057 (red), 0.078 (NIR), to about 0.1 (SWIR). These differences may constitute a significant source of noise for certain applications.

The suitability of a recently published methodology developed to generate Landsat nadir BRDF-adjusted reflectance (NBAR) was examined for Sentinel-2A application. The methodology uses fixed MODIS BRDF spectral parameters and is attractive because it has little sensitivity to the land cover type, condition, or surface disturbance and can be derived in a computationally efficient manner globally. It was applied to the southern Africa Sentinel-2A data and shown to reduce Sentinel-2A BRDF effects. The average difference between the reflectance in the forward and backward scatter directions at the Sentinel-2A scan edges was smaller in the NBAR data than in the corresponding surface reflectance data. Residual BRDF effects in the Sentinel-2A NBAR data occurred likely because of atmospheric correction and sensor calibration errors and inadequacies in the NBAR derivation approach. These issues are discussed with recommendations for future research including global and red-edge Sentinel-2A NBAR derivation that were not considered in this study.

© 2017 The Authors. Published by Elsevier Inc. This is an open access article under the CC BY-NC-ND license (<http://creativecommons.org/licenses/by-nc-nd/4.0/>).

1. Introduction

The potential for near daily medium spatial resolution optical wavelength remote sensing has been advanced by the availability of European Space Agency (ESA) Sentinel-2A data with continuity provided by the Sentinel-2B satellite (Drusch et al., 2012), and NASA USGS Landsat-8 data with continuity provided by a planned Landsat-9

satellite (Loveland and Irons, 2016). The combined utility of the Sentinel-2 multi spectral instrument (MSI) (Drusch et al., 2012) and Landsat-8 and -9 Operational Land Imager (OLI) (Irons et al., 2012) data for science and applications is well recognized (Roy et al., 2014). Both remote sensing systems are in sun-synchronous low earth polar orbits and acquire images at view angles $\pm 10.3^\circ$ (Sentinel-2) and $\pm 7.5^\circ$ (Landsat) from nadir that result in directional reflectance effects over non-Lambertian surfaces. These effects, described by the bidirectional reflectance distribution function (BRDF) (units of sr^{-1}), should be minimized to enable reliable sensor data comparison, mapping of surface features, detection of surface change through space and/or

^{*} Corresponding author.

E-mail address: david.roy@sdstate.edu (D.P. Roy).

time, and to provide consistent data. BRDF effects are relatively small over the Landsat 15° sensor field of view (Roy et al., 2008, 2016a; Flood et al., 2013; Gao et al., 2014) but are expected to be greater for Sentinel-2 data due to the wider 20.6° sensor field of view.

This paper examines the magnitude of Sentinel-2A view zenith BRDF effects observed for a large amount of data acquired over two ten day periods across southern Africa acquired in the solar principal and orthogonal planes. Recently, an empirical c-factor approach was published that provides consistent Landsat view angle corrections to provide nadir BRDF-adjusted reflectance (NBAR) (Roy et al., 2016a). Because the BRDF shapes of different terrestrial surfaces are sufficiently similar over the narrow 15° Landsat field of view, a fixed global set of MODIS BRDF spectral model parameters was found to be adequate for Landsat NBAR derivation with little sensitivity to the land cover type, condition, or surface disturbance (Roy et al., 2016a). The application of this general methodology to Sentinel-2A data is evaluated. Specifically, the reflectance differences between adjacent overlapping Sentinel-2A swaths in the forward and backward scatter directions are quantified for both before (surface reflectance) and after BRDF correction (NBAR).

The satellite data and pre-processing are first described. The pre-processing was challenging due to a Sentinel-2A misregistration issue that was present in the first year of data and also due to the need to reproject different overlapping orbits of data into the same coordinate system. Both top of atmosphere (TOA) and atmospherically corrected, i.e., surface reflectance data were considered. The evaluation methods, that are similar to those described in Roy et al. (2016a), are then described. This is followed by the results that include a quantification of the magnitude of Sentinel-2A view zenith BRDF effects, the efficacy of the NBAR derivation, and a qualitative demonstration of BRDF effects in Sentinel-2A surface reflectance and the correction to surface NBAR. The paper concludes with a discussion and recommendations for future research.

2. Data

2.1. Sentinel-2A data

Sentinel-2A geolocated top of atmosphere (TOA) reflectance (L1C) products were acquired from the Copernicus Open Access Hub that includes an interactive graphical user interface for searching and quicklook visualization (<https://scihub.copernicus.eu/>). The Sentinel-2A MSI has 13 reflective wavelength (433 nm to 2190 nm) spectral bands; four 10 m visible and near-infrared bands, six 20 m red edge, near-infrared and short wave infrared bands, and three 60 m bands (Drusch et al., 2012). In this study the 10 m blue (490 nm), green (560 nm), red (665 nm), near-infrared (NIR) (842 nm) and the 20 m short wave infrared (SWIR) bands (1610 and 2190 nm) were used.

These bands were selected because they have spectrally similar MODIS bands and so spectral BRDF model parameters (Table 1) needed for the BRDF normalization method. The three 60 m MSI bands were not used because they are not designed for land surface monitoring (Drusch et al., 2012). The red edge bands were not considered and the issues for red edge band BRDF normalization are discussed in the conclusion.

The Sentinel-2A MSI has a 20.6° field of view and senses a 290 km swath from a sun-synchronous 786 km polar orbit to provide global coverage every 10 days (Drusch et al., 2012). To ensure that a range of surface BRDFs were examined, Sentinel-2A data acquired over a large area, approximately 20° × 10°, over southern Africa covering most of Namibia and Botswana, the northern half of South Africa, the southern half of Zimbabwe, and south western Mozambique, were used (Fig. 1). BRDF effects are dependent on the physical arrangement and optical properties of the surface components and may change with the land cover type and condition (Roberts, 2001). Analysis of the Collection 5 MODIS land cover product, which classifies each 500 m pixel into one of 17 International Geosphere-Biosphere Program (IGBP) classes (Friedl et al., 2010) indicates that the study area is predominantly composed of open shrublands (44.7%), savannas (24.2%), grasslands (11.9%), and barren or sparsely vegetated (8.6%) land covers but also contains *all* of the other IGBP land cover classes except for the evergreen needleleaf and the snow and ice classes. The generality of the paper findings with respect to land cover and condition are discussed further at the end of this paper.

The Sentinel-2A data from adjacent laterally overlapping orbit swaths are sensed in the forward and backward scatter directions and this pattern alternates with longitude, i.e., the forward and backward scattering orientation alternates between the red and blue orbits illustrated in Fig. 1. It is established, both theoretically and by direct measurement, that BRDF effects over a uniform surface are greatest in the solar principal and least in the orthogonal plane (Kimes, 1983; Hapke et al., 1996; Hauteœur and Leroy, 1998; Sandmeier et al., 1998; Chopping, 2000). Consequently, Sentinel-2A data acquired in two 10-day periods in January and April 2016 were used as they were acquired with quite different solar geometry close to the solar principal and orthogonal planes respectively (Fig. 2). In both months the Sentinel-2A data were acquired with mean view azimuths of 101.43° (backscatter) and 285.08° (forward scatter). For the January data the mean solar azimuth and zenith was 93.31° and 25.33°. For the April data the mean solar azimuth and zenith was 40.55° and 42.41°. These months were also selected because they occur in the southern hemisphere summer and autumn when the vegetation is green and starting to dry respectively but not when there is extensive biomass burning that produces smoke aerosols that are hard to reliably atmospherically correct (Swap et al., 2002; Archibald et al., 2010).

For each selected 10-day period eight orbit overpasses were used (Fig. 1). The UTC sensor acquisition time for these orbits varied from

Table 1
Sentinel-2A and spectrally equivalent MODIS land bands (band central wavelengths in parentheses with bandwidths underneath) and the corresponding MODIS spectral BRDF model parameters $f_{iso}(\lambda)$, $f_{vol}(\lambda)$ and $f_{geo}(\lambda)$ (reproduced from Table 5 of Roy et al., 2016a).

Sentinel-2A band (Drusch et al., 2012)	MODIS band (Barnes et al., 1998)	f_{iso}	f_{geo}	f_{vol}
2 (blue, 490 nm) 65 nm	3 (blue, 469 nm) 20 nm	0.0774	0.0079	0.0372
3 (green, 560 nm) 35 nm	4 (green, 555 nm) 20 nm	0.1306	0.0178	0.0580
4 (red, 665 nm) 30 nm	1 (red, 645 nm) 50 nm	0.1690	0.0227	0.0574
8 (NIR, 842 nm) 115 nm	2 (NIR, 858 nm) 35 nm	0.3093	0.0330	0.1535
11 (SWIR, 1610 nm) 90 nm	6 (SWIR, 1641 nm) 24 nm	0.3430	0.0453	0.1154
12 (SWIR, 2190 nm) 180 nm	7 (SWIR, 2130 nm) 50 nm	0.2658	0.0387	0.0639

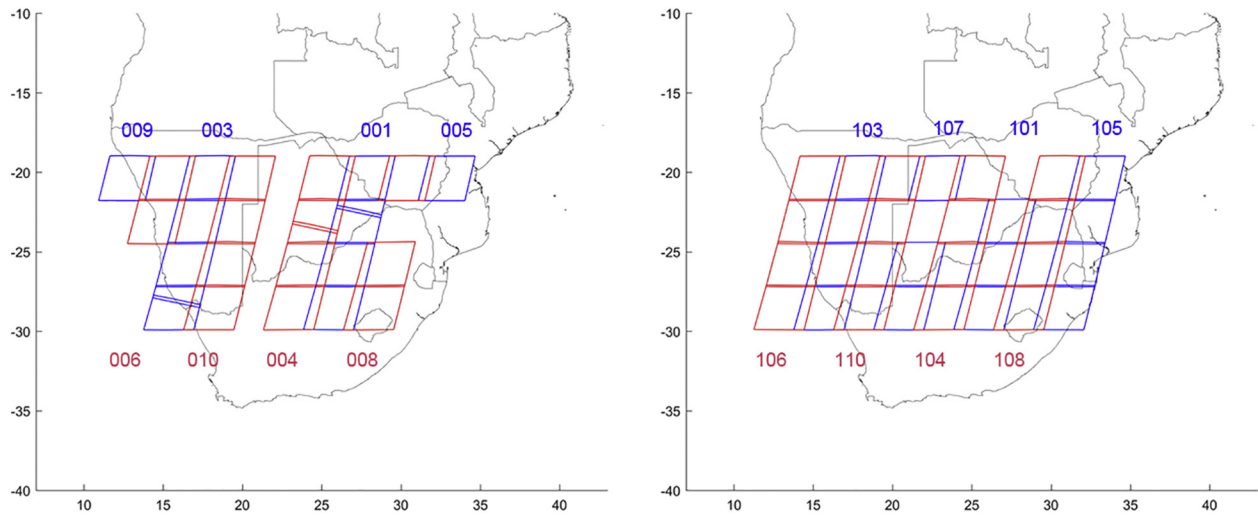


Fig. 1. Geographic locations of the Sentinel-2A data for January 1–10, 2016 (left) and April 10–19, 2016 (right) over southern Africa. The blue and red colors show the different orbit swaths (approximately 290 km across track) with the day of year of each orbit shown by a three digit number. Laterally overlapping orbit swaths are always acquired in the forward and backward scatter directions and were considered in the analysis. Some orbit data were discarded (they are not illustrated) by the data registration pre-processing (Section 3.4) due primarily to persistent cloud cover. (For interpretation of the references to color in this figure legend, the reader is referred to the web version of this article.)

07.42 to 09.03 (January) and from 07.25 to 08.50 (April). Over the study area the Sentinel-2A orbit swath edges overlap every 3 or 7 days. The solar zenith changed in the 3 or 7 day separation by no more than 4.23° (January) and 9.67° (April) at the Sentinel-2A overpass time.

2.2. Global MODIS spectral BRDF model parameters

In this study the approach used to provide Landsat nadir BRDF-adjusted reflectance (NBAR) (Roy et al., 2008, 2016a) was applied to the Sentinel-2A data. The NBAR is derived as the product of the observed satellite reflectance and the ratio of the reflectances modeled using Moderate Resolution Imaging Spectroradiometer (MODIS) BRDF spectral model parameters for the observed and for a nadir view and specified solar zenith geometry (Section 4.2). A fixed set of BRDF spectral model parameters, derived by averaging a global year of all the highest quality snow-free MODIS 500 m BRDF product values ($>15,000$ million values), was provided so users may implement the described Landsat NBAR generation method (Roy et al., 2016a). The same global parameters are summarized in Table 1 with the corresponding Sentinel-2A and MODIS bands shown for reference.

3. Data pre-processing

3.1. Atmospheric correction

The Sentinel-2A L1C data are provided as top of atmosphere (TOA) reflectance. In this study, both TOA and surface reflectance data were considered to examine differences in the observed BRDF. The Sentinel-2A data were atmospherically corrected to surface reflectance using the SEN2COR radiative transfer atmospheric correction code (Version 2.3.0, November 25th, 2016 release) run using the default parameter settings applied independently to each L1C tile (Müller-Wilm, 2016). The SEN2COR code also produces a 20 m scene and cloud classification that was used to screen bad quality pixels. All Sentinel-2A pixels labelled as cloudy (either low, medium or high probability or thin cirrus), saturated, or snow, were discarded. A quantitative validation of the SEN2COR products has not been published.

3.2. Per-pixel solar and view geometry calculation

The Sentinel-2A L1C data are provided in the Universal Transverse Mercator (UTM) map projection (ESA, 2015) in 109×109 km tiles

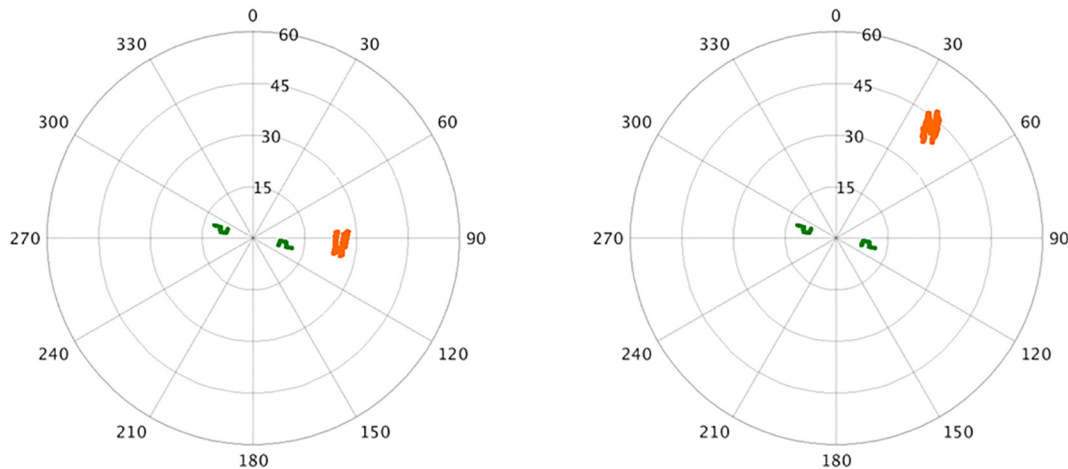


Fig. 2. Polar plots illustrating the solar (orange) and view (green) geometry of the Sentinel-2A data for January 1–10, 2016 (left) and April 10–19, 2016 (right). The radial straight lines show azimuth spaced every 30° and the circles show zenith spaced every 15° . (For interpretation of the references to color in this figure legend, the reader is referred to the web version of this article.)

(Roy et al., 2016b). The solar geometry and view geometry are stored in XML metadata as 23×23 grids with a 5 km grid spacing. There is one solar zenith and solar azimuth grid per tile. However, due to the push-broom sensor design, a view zenith and view azimuth grid is defined for each of the 12 MSI detectors and for each spectral band. In this study the solar and view angles were derived for any Sentinel-2 pixel location by bilinear interpolation from the 5 km grid values.

3.3. Reprojection

Adjacent L1C tiles from the same MSI swath overlap spatially and may be defined in different UTM zones, i.e., in separate map projections (Roy et al., 2016b). In order to be able to compare the different overlapping swaths of Sentinel-2A data each orbit was reprojected independently into the MODIS land product equal area sinusoidal map projection (Wolfe et al., 1998). The global Web Enabled Landsat (WELD) product tiling system that nests 7×7 global WELD tiles within each MODIS $10^\circ \times 10^\circ$ tile was used (Roy et al., 2016b). To handle the different Sentinel-2A band resolutions the data were resampled to 30 m resolution. Specifically, each 30 m pixel location (sinusoidal coordinates) across a global WELD tile was projected into the Sentinel-2 L1C tiles (UTM coordinates) taking care to use the correct L1C tile UTM zone (Roy et al., 2016b). Then the Sentinel-2A TOA reflectance, surface reflectance, solar and viewing geometry angles, and the cloud, saturation, and snow state information were resampled by nearest neighbor resampling. This was undertaken independently for each orbit of data. Each global WELD tile was composed of 5295×5295 30 m pixels.

3.4. Registration

The Sentinel-2A geolocation performance specification is 12.5 m (3σ) (Languille et al., 2015). Our examination of Sentinel-2A L1C data acquired every 10 days over the same location indicated that the data were aligned within this performance specification. This was also found in other studies (Huang et al., 2016). However, when the data in the overlapping Sentinel-2 swath edges were compared, i.e., data acquired 3 or 7 days apart, all the overlapping orbit swath data were found to be mis-registered by typically more than 30 m and up to 100 m. It transpired that this was due to a Sentinel-2A satellite yaw orientation knowledge error that was not rectified in the Sentinel-2A L1C data processing until Summer 2016 (personal communication, December 5th, 2016, Ferran Gascon, ESA). Therefore the Sentinel-2A data were registered using the following steps.

The Global WELD tile projected NIR data for one set of orbit tiles (orbit locations shown as blue in Fig. 1) were considered as the reference data and the adjacent overlapping orbit tiles (shown as red in Fig. 1) were considered as the target data. The target data were registered to the reference data using an automated feature and area-based least squares matching approach that provides sub-pixel precision matching when applied to Sentinel-2A and Landsat-8 data (Yan et al., 2016). A second order polynomial transformation was used:

$$\begin{aligned} x_{ref} &= a_0 + a_1 x_{target} + a_2 y_{target} + a_3 x_{target} \times x_{target} + a_4 x_{target} \times y_{target} + a_5 y_{target} \times y_{target} \\ y_{ref} &= b_0 + b_1 x_{target} + b_2 y_{target} + b_3 x_{target} \times x_{target} + b_4 x_{target} \times y_{target} + b_5 y_{target} \times y_{target} \end{aligned} \quad (1)$$

where (x_{ref}, y_{ref}) are the column and row global WELD tile reference pixel coordinates, (x_{target}, y_{target}) are the corresponding target global WELD tile pixel coordinates, and a_i and b_i are the polynomial transformation coefficients. If the root-mean-square error used to fit Eq. (1) (see Yan et al., 2016) was >15 m then the data were not registered and the tile pair was discarded; this occurred due to cloud obscuration. Otherwise, the Sentinel-2A data were reprojected (Section 3.3) including the tile pixel coordinate transformation adjustment provided by Eq. (1). In this way the data used in this study were well registered but were not resampled twice.

3.5. Data extraction

The Sentinel-2A sensor overlap region between adjacent orbits is acquired in the forward scattering direction from one orbit and the backward scattering direction from the other orbit. In this study, every pair of sensor reflectance values defined in the overlap at the same sinusoidal 30 m pixel location was extracted. Only values that were not labelled as cloudy (either low, medium or high probability or thin cirrus), saturated, or snow (Section 3.1) were used. The 3 or 7 day separation between observations of the same pixel location is sufficiently long that changes in the surface condition may have occurred and the atmosphere is quite likely to have changed. To remove the effects of these changes, and also any residual cloud or shadow contamination occurring in either observation, the following filtering was applied to reject pairs if:

$$\frac{|NDVI^{forward} - NDVI^{backward}|}{|NDVI^{forward} + NDVI^{backward}|} > 0.15 \quad \text{OR} \quad \frac{|\rho_{blue}^{forward} - \rho_{blue}^{backward}|}{|\rho_{blue}^{forward} + \rho_{blue}^{backward}|} > 0.5 \quad (2)$$

where the superscripts denote the pair of observations of the 30 m global WELD tile pixel sensed in the forward and backward scattering directions, the NDVI is the Normalized Difference Vegetation Index defined as the difference between the NIR (band 8) and red (band 4) TOA reflectance divided by their sum, and ρ_{blue} is the TOA blue (band 2) reflectance. This filtering is the same as that used to compare overlapping Landsat orbits sensed over the United States (Roy et al., 2016a). It removes a large proportion of the data, but given the large amount of data considered this is preferable to retaining Sentinel-2A overlapping pairs that contain surface or atmospheric changes.

4. Analysis methodology

4.1. Quantification of Sentinel-2A directional reflectance effects

The reflectance difference between each pair of Sentinel-2A values observed in the swath image overlap zone (i.e., where the red and blue swaths in Fig. 1 overlap) were first examined to provide insights into the magnitude of Sentinel-2A view zenith BRDF effects. Following the same approach as Roy et al. (2016a) the mean absolute reflectance difference, and also the relative absolute percentage reflectance difference, were derived for every pair of overlapping observations across southern Africa as:

$$\overline{\Delta\rho_\lambda} = \frac{\sum_{i=1}^n |\rho_i^{forward,\lambda} - \rho_i^{backward,\lambda}|}{n} \quad (3)$$

$$\overline{\Delta\rho_\lambda^*} = \left(\frac{\sum_{i=1}^n 2|\rho_i^{forward,\lambda} - \rho_i^{backward,\lambda}|}{n(|\rho_i^{forward,\lambda} + \rho_i^{backward,\lambda}|)} \right) \times 100 \quad (4)$$

where $\overline{\Delta\rho_\lambda}$ and $\overline{\Delta\rho_\lambda^*}$ are the mean absolute and the relative absolute percentage reflectance differences respectively, $\rho_i^{forward,\lambda}$ and $\rho_i^{backward,\lambda}$ is a pair of forward and backward reflectance values and there are n pairs for Sentinel-2A wavelength λ . As each pair is sensed with similar solar geometry but different viewing geometry, specifically the reflectance is sensed in the forward scattering direction from one swath edge and the backward scattering direction from the other swath edge, these measures provide an indication of view zenith Sentinel-2A BRDF effects. This analysis was undertaken for the TOA and surface reflectance data separately.

4.2. Sentinel-2A NBAR derivation

The reflectances for each pair of Sentinel-2A values observed in the forward and backward scattering directions in the swath overlap zone were normalized to nadir BRDF-adjusted reflectance (NBAR) equivalents. The NBAR was derived as the product of the observed reflectance and an adjustment c-factor defined by the ratio of reflectances modeled using MODIS BRDF spectral model parameters for the observed and a fixed nadir view geometry (Roy et al., 2008, 2016a) as:

$$NBAR_{\lambda}(\theta_v = 0, \theta_s = k) = c_{\lambda} \times \rho_{\lambda}(\theta_v = \theta_v^{Sentinel}, \theta_s = \theta_s^{Sentinel}) \quad (5)$$

$$c_{\lambda} = \frac{\hat{\rho}_{\lambda}^{MODIS}(\theta_v = 0, \theta_s = k)}{\hat{\rho}_{\lambda}^{MODIS}(\theta_v = \theta_v^{Sentinel}, \theta_s = \theta_s^{Sentinel})}$$

where ρ_{λ} is the Sentinel-2A reflectance (for either the forward or backward scattering direction) sensed with view zenith ($\theta_v^{Sentinel}$) and solar zenith ($\theta_s^{Sentinel}$) for wavelength λ , and $NBAR_{\lambda}$ is the nadir BRDF-adjusted reflectance equivalent estimated for a solar zenith angle ($\theta_s = k$ set as the average solar zenith of the pair of forward and backward scattering observations) for a nadir view zenith ($\theta_v = 0$). The $\hat{\rho}_{\lambda}^{MODIS}$ values in Eq. (5) were estimated using the standard MODIS Ross-Thick/Li-Sparse-Reciprocal model (Roujean et al., 1992; Schaaf et al., 2002) as:

$$\hat{\rho}_{\lambda}^{MODIS}(\Omega, \Omega') = f_{iso}(\lambda) + f_{vol}(\lambda)K_{vol}(\Omega, \Omega') + f_{geo}(\lambda)K_{geo}(\Omega, \Omega') \quad (6)$$

where $\hat{\rho}_{\lambda}^{MODIS}(\Omega, \Omega')$ is the MODIS spectral reflectance for wavelength λ_{MODIS} , for viewing vector Ω (view zenith and azimuth angles) and solar illumination vector Ω' (solar zenith and azimuth angles), $K_{vol}(\Omega, \Omega')$ and $K_{geo}(\Omega, \Omega')$ are volumetric scattering and geometric-optical model kernels respectively, and $f_{iso}(\lambda_{MODIS})$, $f_{vol}(\lambda_{MODIS})$, $f_{geo}(\lambda_{MODIS})$ are the fixed BRDF spectral model parameters derived from the global year of highest quality snow-free MODIS BRDF product values defined in Table 1. The kernels depend only on the sun-view geometry (Ω, Ω') (Roujean et al., 1992; Schaaf et al., 2002).

4.3. Sentinel NBAR evaluation

As noted in Roy et al. (2016a) if the BRDF normalization is reliable then the NBAR values of each pair of Sentinel-2A observations in the swath overlap zone should be similar. To examine this, the mean and relative absolute percentage NBAR differences were derived in the same way as Eqs. (3) and (4) as:

$$\overline{NBAR}_{\lambda} = \frac{\sum_{i=1}^n |NBAR_i^{forward, \lambda} - NBAR_i^{backward, \lambda}|}{n} \quad (7)$$

$$\overline{NBAR}_{\lambda}^* = \left(\frac{\sum_{i=1}^n 2|NBAR_i^{forward, \lambda} - NBAR_i^{backward, \lambda}|}{n |NBAR_i^{forward, \lambda} + NBAR_i^{backward, \lambda}|} \right) \times 100 \quad (8)$$

where $\overline{NBAR}_{\lambda}$ is the mean absolute NBAR difference derived for spectral band λ from n pairs of forward and back scatter NBAR values derived as Eq. (5), and $\overline{NBAR}_{\lambda}^*$ is the mean absolute relative percentage NBAR difference.

Following the analysis methodology described in Roy et al. (2016a) spectral scatter plots and ordinary least squares (OLS) regression fits of the differences between the observed reflectance pairs and also the NBAR pairs as a function of the view zenith angle were generated independently for each Sentinel-2A band considered (Table 1). The slopes of the OLS regressions were derived to quantify the average spectral BRDF effect across the Sentinel-2A field of view. The significance of the OLS regressions and their goodness of fit were defined by the regression

overall F-statistic p-value and the coefficient of determination (r^2) respectively. The average difference between Sentinel-2A reflectance in the forward and backward scatter directions at the scan edges, termed here for convenience as the B–F difference, was derived as the product of the OLS slope term and the maximum observed view zenith range.

5. Results

5.1. Quantification of Sentinel-2A bi-directional reflectance effects

Fig. 3 shows scatterplots of Sentinel-2A TOA red reflectance difference (left column) and TOA NIR reflectance difference (right column) as a function of view zenith for the January data. The plots were generated using all the data extracted from each overlapping swath over southern Africa that were not labelled as cloudy (either low, medium or high probability or thin cirrus), saturated, or snow. The TOA reflectance differences for each pair of forward and backward scatter observations were derived as the blue minus the red orbit data (Fig. 1 left) and plotted as function of the blue orbit view zenith angles. Fig. 4 shows the same scatterplots as Fig. 3 but generated after application of the Eq. (2) filtering to remove the effect of land and/or surface changes in the 3 or 7 day separation between each pair of pixel observations. The Eq. (2) filtering removed 32% of the January data, from 9,779,119 (Fig. 3) to 6,600,685 (Fig. 4) pairs of forward and back scatter reflectance values, and reduced the scatter in the plotted data (the r^2 values increased from approximately 0.5 to 0.7). Similarly, the Eq. (2) filtering removed 24% of the April data, from 14,062,474 to 10,656,197 pairs of forward and back scatter reflectance values, and reduced the scatter in the plotted data. For both months, the Eq. (2) filtering only marginally changed the OLS regression lines, with differences in the OLS slope terms occurring in the fourth decimal place only. Consequently, the filtering does not overly influence the results reported in this paper. The rest of the results are for the data subject to all the filtering described in Section 3, i.e., after removing Sentinel-2A data labelled as cloudy (either low, medium or high probability or thin cirrus), saturated, or snow, and after application of Eq. (2).

In Figs. 3 and 4 (and subsequent figures) there are no plotted data with absolute values of view zenith $< 7.61^\circ$. This is due to the Sentinel-2A orbit and sensing geometry over the study area that cause only the swath edges to overlap (Fig. 1). The maximum view zenith for both the January and April data was 11.93° and the maximum observed view zenith range was 23.86° (which is greater than the 20.6° field of view due to earth curvature). There is an evident Sentinel-2A view zenith BRDF effect across the field of view with a pronounced OLS regression line slope in both the red and NIR bands that is quantified below.

Fig. 5 shows the same results as Fig. 4 but for the surface reflectance. The impact of the atmospheric correction is to increase the figure y-axes data range, i.e., increase the reflectance differences between the forward and backward scatter observations. This is expected. Atmospheric correction has been observed to increase the scatter in reflectance relative to TOA reflectance in large area Landsat atmospheric correction studies (Ju et al., 2012; Roy et al., 2014; Claverie et al., 2015) and occurs primarily because Rayleigh and aerosol backscatter increase the TOA reflectance over dark surfaces and aerosol absorption decreases the TOA reflectance over bright surfaces (Kaufman and Sendra, 1988; Tanre et al., 1981). The slope of the OLS regression lines is slightly greater in the atmospherically corrected data, i.e., after atmospheric correction the surface BRDF is slightly more pronounced. This is known and is because atmospheric constituents usually smooth the angular dependence of non-Lambertian surface reflectance (Lee and Kaufman, 1986; Rahman, 1996; Hu et al., 1999; Franch et al., 2013).

Fig. 6 shows the same type of plots as Fig. 5 but for the April data and for a total of 10,656,197 pairs of forward and back scatter reflectance difference values. Comparing the January (Fig. 5) and April (Fig. 6)

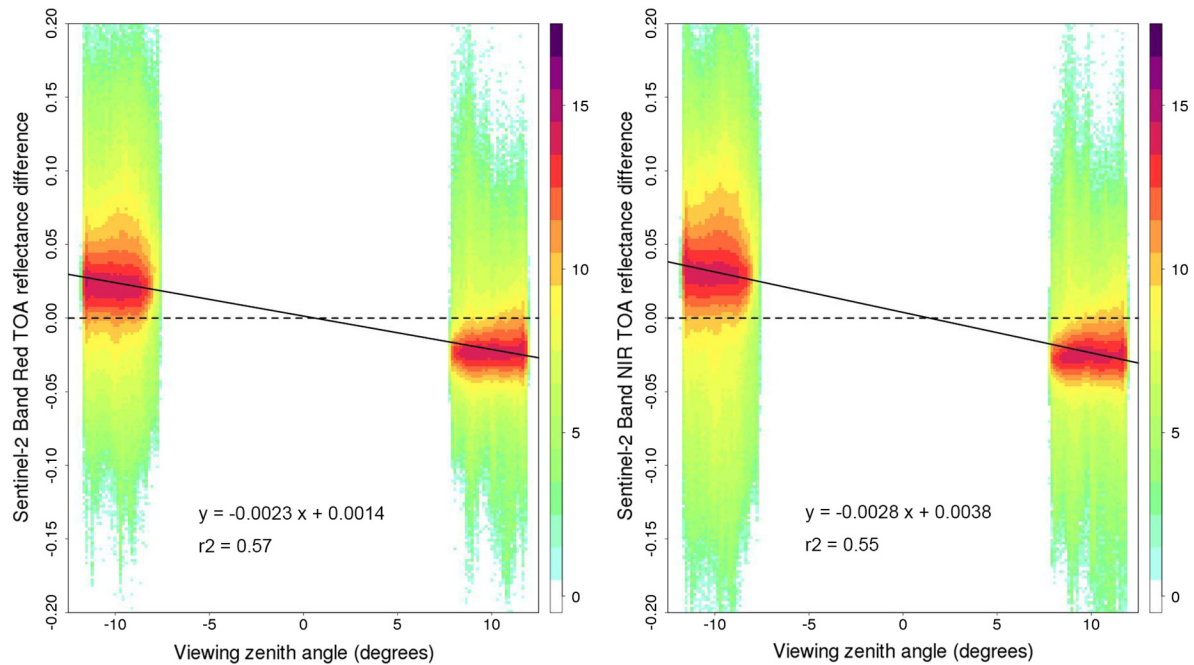


Fig. 3. Scatterplots of Sentinel-2A top of atmosphere (TOA) red (left) and NIR (right) reflectance differences in the southern Africa January swath image overlap zones plotted against view zenith. Differences for a total of 9,779,119 pairs of forward and back scatter TOA reflectance values (blue orbit minus red orbit reflectance) plotted against blue orbit view zenith angles (positive/negative view zenith angles correspond to forward/backward scattering in the blue orbit, see Fig. 1). These data were *not* filtered with Eq. (2) to remove the effect of land and/or surface changes in the 3 or 7 day separation between each pair of pixel observations. The plot colors show the relative frequency of occurrence of similar difference values (with a \log_2 scale). The solid lines show ordinary least squares (OLS) linear regression fits of these data. (For interpretation of the references to color in this figure legend, the reader is referred to the web version of this article.)

scatterplots clearly indicate that the BRDF effects are greater in January than April. This may reflect surface differences between the two months, for example, associated with changes in the vegetation cover and condition from Summer to Autumn that have different BRDF, but more likely reflect the different sun-surface-sensor orientation between the two months of Sentinel-2A data. The January data were sensed close to the solar principal plane (Fig. 2. left) and the April data

were sensed close to the orthogonal plane (Fig. 2. right) where BRDF effects are more and less pronounced, respectively. The range of reflectance differences (y-axis values) are more dissimilar either side of nadir in January (Fig. 4) than in April (Fig. 5). This is likely because the different land covers and conditions across the study area exhibit a greater range of surface reflectance anisotropy closer to the solar principle plane.

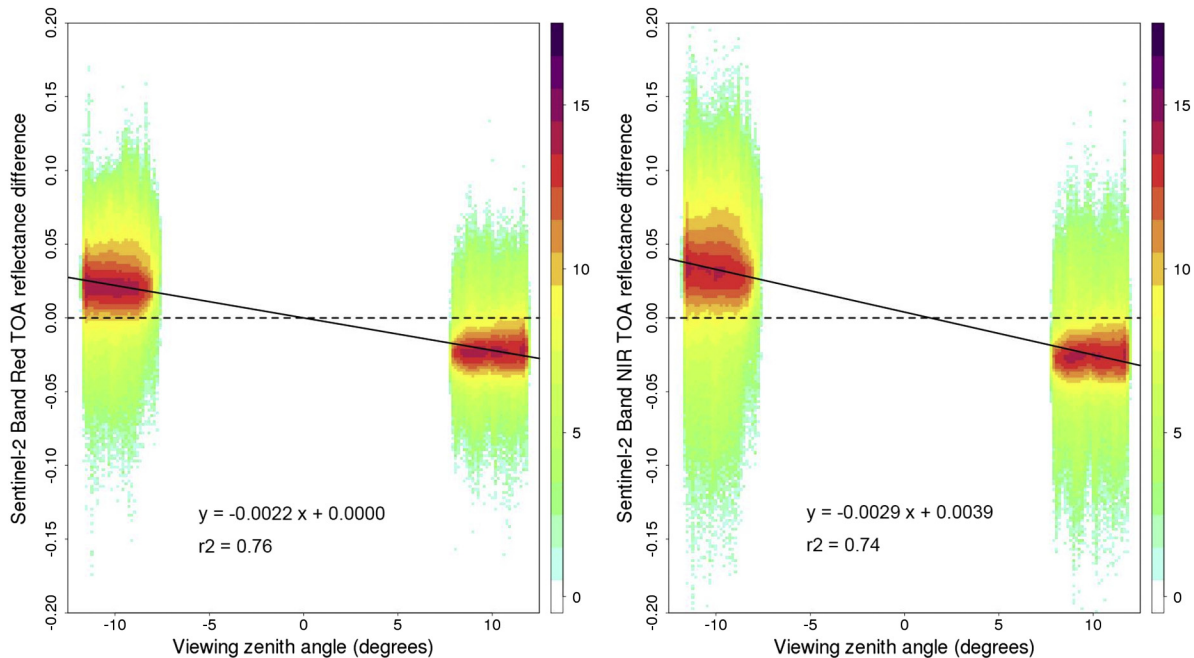


Fig. 4. Scatterplots of Sentinel-2A top of atmosphere (TOA) red (left) and NIR (right) reflectance differences in the southern Africa January swath image overlap zones plotted against blue orbit view zenith angles. Results as Fig. 3 but for the data filtered by Eq. (2) to remove the effect of land and/or surface changes in the 3 or 7 day separation between each pair of pixel observations. Differences for a total of 6,600,685 pairs of forward and back scatter TOA reflectance values.

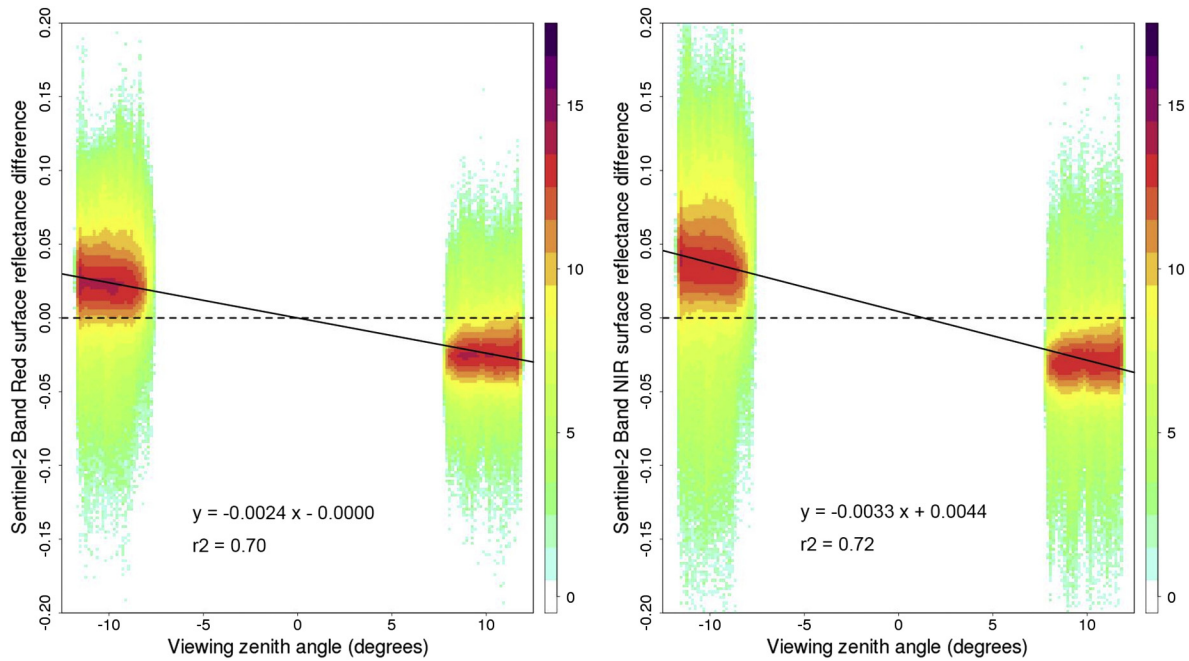


Fig. 5. Scatterplots of Sentinel-2A surface red (left) and NIR (right) reflectance differences in the southern Africa January swath image overlap zones (Fig. 1 left) plotted against view zenith. Differences for a total of 6,600,685 pairs of forward and back scatter surface reflectance values (blue orbit minus red orbit reflectance) plotted against blue orbit view zenith angles (positive/negative view zenith angles correspond to forward/backward scattering in the blue orbit, see Fig. 1 left). The plot colors show the relative frequency of occurrence of similar difference values (with a \log_2 scale). The solid lines show ordinary least squares (OLS) linear regression fits of these data (see Table 4). (For interpretation of the references to color in this figure legend, the reader is referred to the web version of this article.)

Tables 2 and 3 summarize the mean absolute ($\overline{\Delta\rho_\lambda}$ defined by Eq. (3)) and relative absolute percentage ($\overline{\Delta\rho_\lambda^*}$ defined by Eq. (4)) differences between the pairs of forward and backward scatter surface reflectance values for the Sentinel-2A bands. Table 2 shows the results for the TOA reflectance and Table 3 shows the results for the surface reflectance differences. The January data have systematically greater differences

than the April data because the BRDF effects are greater in January than April. The mean absolute difference values, $\overline{\Delta\rho_\lambda}$, are smaller for the visible bands and greater for the other bands. The mean relative absolute difference values, $\overline{\Delta\rho_\lambda^*}$, are normalized by the reflectance magnitude which changes with wavelength, for example, healthy vegetation has high NIR but low red surface reflectance, and so are more

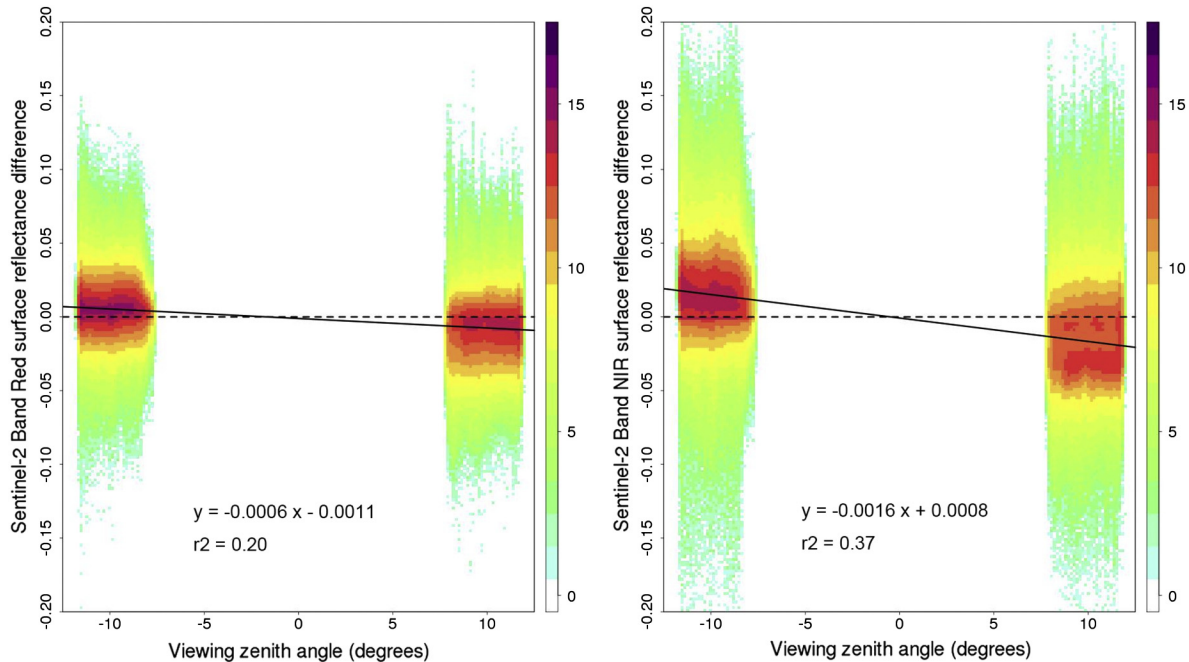


Fig. 6. Scatterplots of Sentinel-2A surface red (left) and NIR (right) reflectance differences in the southern Africa April swath image overlap zones (Fig. 1 right) plotted against view zenith. Differences for a total of 10,656,197 pairs of forward and back scatter surface reflectance values (blue orbit minus red orbit reflectance) plotted against blue orbit view zenith angles (positive/negative view zenith angles correspond to forward/backward scattering in the blue orbit, see Fig. 1 right). The plot colors show the relative frequency of occurrence of similar difference values (with a \log_2 scale). The solid lines show ordinary least squares (OLS) linear regression fits of these data (see Table 4). (For interpretation of the references to colour in this figure legend, the reader is referred to the web version of this article.)

Table 2

Mean absolute reflectance differences $\overline{\Delta\rho_\lambda}$ (Eq. (3)) and mean absolute relative percentage differences $\overline{\Delta\rho_\lambda^*}$ (Eq. (4)) between the pairs of forward and backward scatter Sentinel-2A top of atmosphere (TOA) reflectance values for January (6,600,685 pairs) and April (10,656,197 pairs) in the southern Africa overlapping orbit swaths (locations shown in Fig. 1). All data subject to the filtering described in Section 3.

Sentinel-2A band	January		April	
	$\overline{\Delta\rho_\lambda}$	$\overline{\Delta\rho_\lambda^*}$	$\overline{\Delta\rho_\lambda}$	$\overline{\Delta\rho_\lambda^*}$
2 (blue)	0.0184	14.4220	0.0080	7.1498
3 (green)	0.0196	14.3857	0.0078	6.7799
4 (red)	0.0230	13.0344	0.0085	6.5259
8 (NIR)	0.0312	12.4212	0.0164	6.5919
11 (SWIR)	0.0428	12.4745	0.0168	6.9216
12 (SWIR)	0.0347	13.0716	0.0146	8.3013

straightforward to compare among bands than the $\overline{\Delta\rho_\lambda}$ values. For the TOA reflectance data (Table 2) the $\overline{\Delta\rho_\lambda^*}$ values vary among the bands from 12.5% to 14.4% (January) and 6.5% to 8.3% (April). The $\overline{\Delta\rho_\lambda^*}$ values are always greater for the surface reflectance data (Table 3) than for the TOA reflectance data (Table 2) reflecting errors introduced by the atmospheric correction. In particular, the surface $\overline{\Delta\rho_\lambda^*}$ values are much greater than the TOA $\overline{\Delta\rho_\lambda^*}$ values in the blue and green bands and this reflects known atmospheric correction errors at these shorter visible wavelengths (Ju et al., 2012). For the surface reflectance data (Table 2) the $\overline{\Delta\rho_\lambda^*}$ values vary among the bands from 12.8% to 23.2% (January) and 8.1% to 17.0% (April). The remainder of the results are shown for the surface reflectance data.

Table 4 summarizes the OLS regression fits of the differences between the surface reflectance pairs as a function of view zenith (illustrated by solid lines for the red and NIR bands in Figs. 5 and 6). For all the bands the OLS regressions have negative slope terms, $r^2 > 0.5$, and are statistically significant ($p < 0.0001$). The magnitudes of the slopes are greater for January than April reflecting the greater BRDF effects in the January data. The B–F difference, i.e., the OLS slope term multiplied by the maximum observed view zenith range (23.86°) quantifies the average difference between surface reflectance in the forward and backward scatter directions at the sensor scan edges. In January the B–F differences increase with wavelength from 0.035 (blue), 0.047 (green), 0.057 (red), 0.078 (NIR) to about 0.1 (SWIR bands) and are approximately a third smaller for the April data. These Sentinel-2A view zenith BRDF effects are significant and are discussed in the conclusion.

5.2. Evaluation of Sentinel-2A NBAR derived using the MODIS BRDF spectral parameter c-factor approach

Figs. 7 and 8 shows scatterplots of the surface NBAR differences for the January and April data respectively. Comparing these figures with the corresponding surface reflectance difference images (Figs. 5 and 6) illustrate that normalization of the surface reflectance to NBAR reduces the BRDF effects. However, the BRDF normalization is not perfect. Although the April NBAR exhibit almost no residual BRDF effects with OLS regression lines that are near horizontal (Fig. 8), the January NBAR data have evident small residual BRDF effects (Fig. 7).

Table 3

Results as Table 2 but for the surface reflectance data.

Sentinel-2A band	January		April	
	$\overline{\Delta\rho_\lambda}$	$\overline{\Delta\rho_\lambda^*}$	$\overline{\Delta\rho_\lambda}$	$\overline{\Delta\rho_\lambda^*}$
2 (blue)	0.0174	23.2417	0.0086	16.9727
3 (green)	0.0212	17.6659	0.0084	9.6825
4 (red)	0.0254	14.8178	0.0102	10.8389
8 (NIR)	0.0358	12.9200	0.0201	8.2893
11 (SWIR)	0.0483	12.8443	0.0193	8.0719
12 (SWIR)	0.0446	14.0765	0.0176	8.7148

Table 5 summarizes the mean absolute NBAR differences ($\overline{\Delta\text{NBAR}_\lambda}$) and the mean relative absolute percentage NBAR differences ($\overline{\Delta\text{NBAR}_\lambda^*}$) for all the Sentinel-2A bands. Comparison of these difference statistics with the corresponding surface reflectance sensor difference statistics reported in Table 3 reveals that, for all bands and for both months, the NBAR differences are smaller than the corresponding surface reflectance differences. The $\overline{\Delta\text{NBAR}_\lambda^*}$ (Table 5) values, like the $\overline{\Delta\rho_\lambda^*}$ values (Table 3), are greatest for the visible bands, reflecting known atmospheric correction errors at shorter visible wavelengths (Ju et al., 2012). The NBAR differences reported in Table 5 are not zero-valued because of factors including atmospheric correction errors, imperfect sensor calibration, and inadequacies in the c-factor normalization approach. These factors are discussed in the conclusion.

Table 6 summarizes the OLS regression fits of the differences between the surface NBAR pairs as a function of the view zenith angle. The NBAR B–F differences are small varying among the bands from 0.016 to 0.028 (January) and from 0.001 to 0.007 (April). The OLS slope magnitudes and r^2 values, and the magnitude of the B–F NBAR differences (Table 6) are, for all bands and for both the January and April data, smaller than the corresponding values for the surface reflectance data (Table 4). Evidently, the MODIS BRDF spectral parameter c-factor approach systematically reduces Sentinel-2A BRDF effects in the study data.

5.3. Qualitative examination

Figs. 9 and 10 demonstrate qualitatively the BRDF effects in Sentinel-2A true color (red, green, blue) surface reflectance (top left) and the correction to surface NBAR (top right). The arithmetic difference between these data for the red Sentinel-2A band is also shown (bottom left). Results for a WELD tile (Fig. 9) and a detailed spatial subset (Fig. 10) generated by the registration and reprojection (Section 3) of two adjacent Sentinel-2A orbits are shown. The Sentinel-2A data were acquired over a shrubby savanna grassland area encompassing the Botswana and South Africa border and were sensed three days apart in January 2016 (orbits 004 and 001, Fig. 1. left). The data were not temporally composited, rather, to enable clear visualization of the BRDF effects, the western Sentinel-2A swath data were written over the eastern swath data where they overlapped. The western swath was sensed

Table 4

Summary of the ordinary least squares (OLS) linear regressions of the surface reflectance differences illustrated in Figs. 5 and 6 and for the other Sentinel-2A bands. A total of 6,600,685 (January) and 10,656,197 (April) values were used to derive the OLS regressions where Δ = blue orbit minus red orbit surface reflectance and θ_v = blue orbit view zenith angle (see Fig. 1). The OLS regression coefficient of determination (r^2), the OLS regression F-test p-value, and the B-F difference are shown.

Sentinel-2A band	January			April		
	OLS equation	OLS r^2 (p-value)	B-F difference	OLS equation	OLS r^2 (p-value)	B-F difference
2 (blue)	$\Delta = -0.0015 \theta_v + 0.0002$	0.5295 (<0.0001)	0.0354	$\Delta = -0.0002 \theta_v - 0.0008$	0.0374 (<0.0001)	0.0053
3 (green)	$\Delta = -0.0020 \theta_v + 0.0011$	0.6968 (<0.0001)	0.0468	$\Delta = -0.0005 \theta_v - 0.0002$	0.1892 (<0.0001)	0.0122
4 (red)	$\Delta = -0.0024 \theta_v - 0.0000$	0.7030 (<0.0001)	0.0566	$\Delta = -0.0006 \theta_v - 0.0011$	0.2018 (<0.0001)	0.0153
8 (NIR)	$\Delta = -0.0033 \theta_v + 0.0044$	0.7190 (<0.0001)	0.0783	$\Delta = -0.0016 \theta_v - 0.0008$	0.3673 (<0.0001)	0.0377
11 (SWIR)	$\Delta = -0.0044 \theta_v + 0.0072$	0.6902 (<0.0001)	0.1044	$\Delta = -0.0016 \theta_v - 0.0020$	0.3885 (<0.0001)	0.0376
12 (SWIR)	$\Delta = -0.0041 \theta_v + 0.0043$	0.6826 (<0.0001)	0.0967	$\Delta = -0.0014 \theta_v - 0.0024$	0.3746 (<0.0001)	0.0336

January 4th, 2016 in the forward scatter direction and the eastern swath was sensed January 1st, 2016 in the back scatter direction.

Surface reflectance BRDF effects are evident with a pronounced discontinuity (Figs. 9 and 10 top left) along the swath boundary that is oriented approximately NNE to SSW due to the Sentinel-2A orbit geometry (Fig. 1). The eastern Sentinel-2A swath was sensed in the back scatter direction and so has higher surface reflectance, due primarily to shadow-hiding (Hapke et al., 1996), than the western swath that was sensed in the forward scatter direction. The BRDF effects between the forward and backward scattering directions in the two swaths of surface reflectance are reduced in the NBAR data (Figs. 9 and 10 top right). The arithmetic differences between the red band NBAR and red surface reflectance data (Figs. 9 and 10 bottom left) illustrate how the western and eastern orbit NBAR is systematically greater and smaller than the equivalent surface reflectance values respectively and also illustrate the degree of BRDF adjustment provided by the c-factor approach. The mean and standard deviation of the absolute value of this difference across the tile is 0.0074 and 0.0024 respectively. The differences increase closer to the swath boundary as BRDF effects become more pronounced with greater view zenith. Considering all the tile data (Fig. 9 bottom left) the maximum red (NBAR-surface reflectance) value is -0.0624 (Eastern swath) and 0.0395 (Western swath) and occur over the highly reflective clouds due to the multiplicative adjustment provided by Eq. (5).

Fig. 10 shows the same results as Fig. 9 but for a detailed subset. The BRDF effects between the forward and backward scattering directions in the two swaths of surface reflectance (top left) are reduced in the NBAR data (top right). However, the swath boundary is still evident in the NBAR data. The western and eastern Sentinel-2A swaths were sensed with 24.10° and 26.02° solar zenith angles (at the tile center) respectively and the NBAR differences across the swath boundary are not likely to be due to such a small ($<2^\circ$) solar view zenith difference. The illustrated data were not subject to the filtering (Eq. (2)) used to reduce the impact of surface and atmospheric change and so these are likely to be present as the two Sentinel-2A swaths were acquired three days apart. The illustrated subset encompasses an along-track boundary between two Sentinel L1C tiles (oriented WNW to ESE) sensed in the same western orbit. The along-track boundary is not due to surface change but rather is due to residual SEN2COR atmospheric correction errors that are different in the two L1C tiles. These residual atmospheric correction errors are comparable in magnitude to the residual BRDF effects evident in the NBAR data.

6. Conclusion and discussion

The results of this paper demonstrated pronounced Sentinel-2A BRDF effects in the visible, near-infrared and short wave infrared bands. Two ten day periods of Sentinel-2A data over approximately

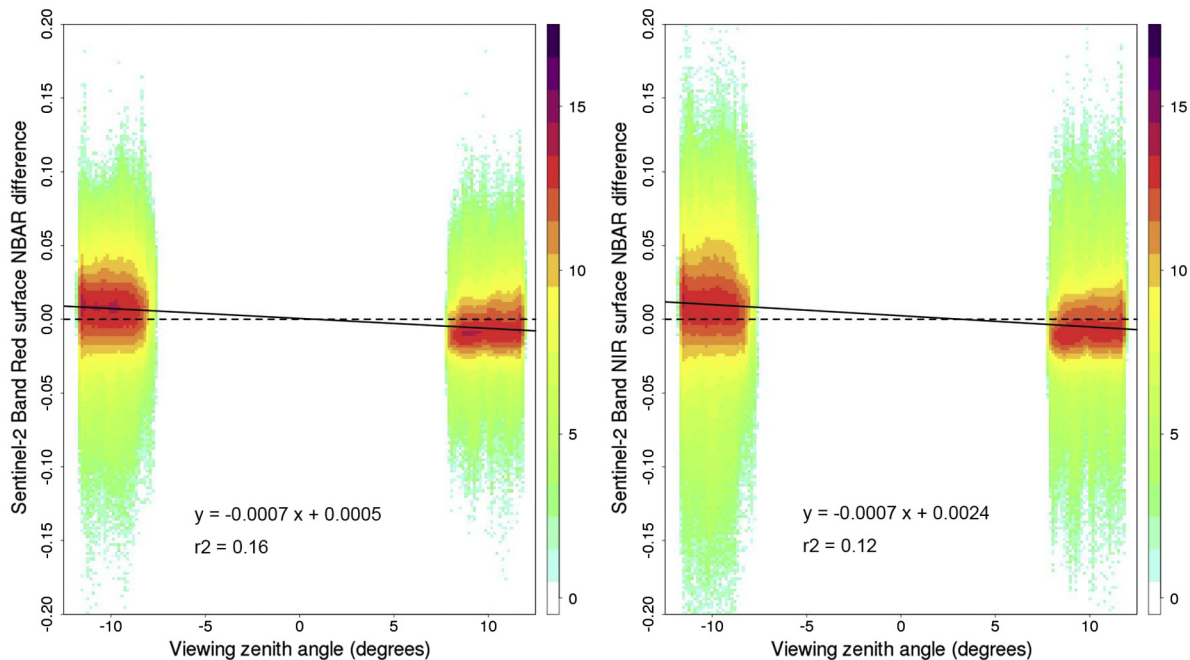


Fig. 7. Scatterplots of Sentinel-2A surface NBAR red (left) and NIR (right) differences in the southern Africa January swath image overlap zones (Fig. 1 left) plotted against view zenith, i.e., the same as Fig. 5 but for NBAR derived from the surface reflectance. The solid lines show ordinary least squares (OLS) linear regression fits of these data (see Table 6).

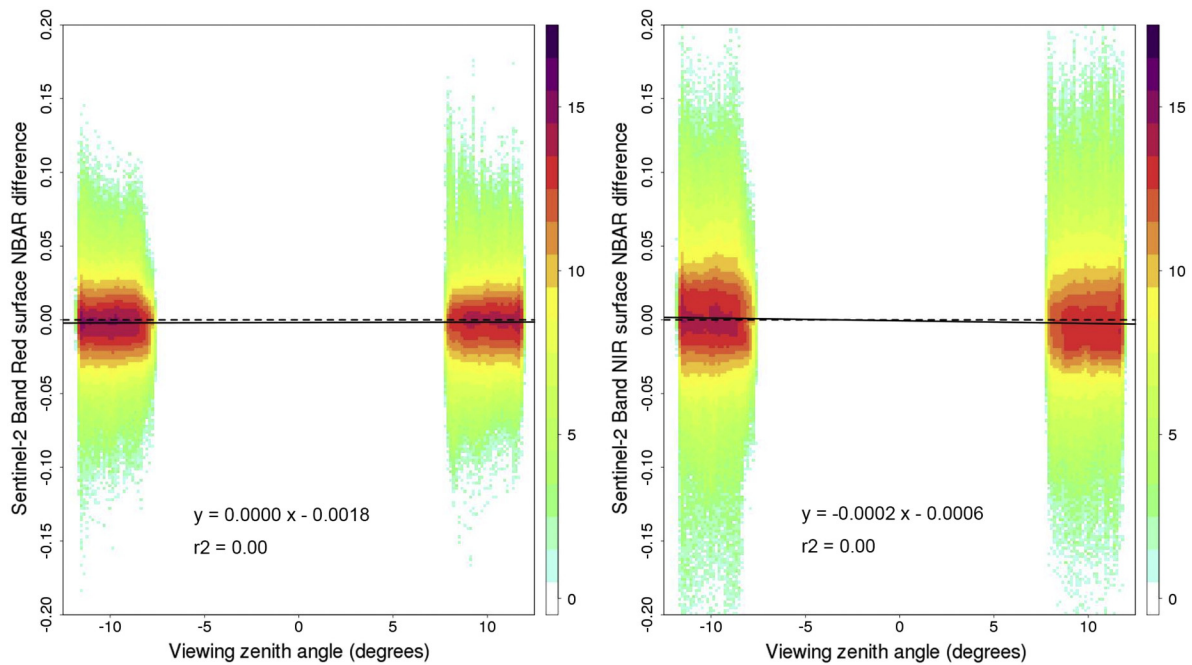


Fig. 8. Scatterplots of Sentinel-2A surface NBAR red (left) and NIR (right) differences in the southern Africa April swath image overlap zones (Fig. 1 right) plotted against view zenith, i.e., the same as Fig. 6 but for NBAR derived from the surface reflectance. The solid lines show ordinary least squares (OLS) linear regression fits of these data (see Table 6).

$20^\circ \times 10^\circ$ of southern Africa were considered. This provided more than 6.6 million (January) and 10.6 million (April) pairs of forward and back scatter reflectance observations extracted from eight overlapping orbits in each period. Following the methodology described in Roy et al. (2016a) spectral scatter plots and ordinary least squares (OLS) linear regression fits of the differences between the observed reflectance pairs as a function of the view zenith angle were generated for each Sentinel-2A band. The B–F difference, derived by multiplying the OLS regression slope term by the maximum observed view zenith range, quantified the average difference between reflectance in the forward and backward scatter directions at the Sentinel-2A scan edges. For the January data (acquired close to the solar principal plane) the surface reflectance B–F differences increased with wavelength from 0.035 (blue), 0.047 (green), 0.057 (red), 0.078 (NIR), to about 0.1 (SWIR bands). For the April data (acquired close to the orthogonal principal plane) the surface reflectance B–F differences were approximately three times smaller. These values are greater than reported with respect to conterminous United States Landsat data (Roy et al., 2016a) most likely because the Landsat data were acquired over a smaller field of view and further from the solar principal plane. Evidently, research examining Sentinel-2 BRDF, or testing BRDF normalization methods, should consider a representative variation in solar and viewing geometry and include data

acquired close to the solar principal plane. The Sentinel-2A BRDF effects described in this paper are quite large and may constitute a significant source of noise for certain applications. For example, the average 0.057 red band difference between the Sentinel-2A swath edge forward and backward scatter directions is comparable to more than half the red reflectance range among different vegetation types.

The MODIS BRDF spectral parameter c-factor approach, developed to derive Landsat NBAR (Roy et al., 2016a), was applied to the Sentinel-2A data and reduced BRDF effects. Notably, the Sentinel-2A NBAR B–F differences were, for all bands and for the January and April data, smaller than the corresponding surface reflectance difference values. The differences were greater for the January data (that had more pronounced surface reflectance BRDF effects) and varied among bands from a minimum of 0.016 (red) to 0.028 (SWIR) and were less than 0.01 for all bands of the April data. The BRDF normalization was not perfect because of factors including inadequacies in the c-factor normalization approach and atmospheric correction and sensor calibration errors that are discussed below.

Several factors may reduce the efficacy of the MODIS BRDF spectral parameter c-factor normalization approach for Sentinel-2A application. First, the approach is based on the shape and not the magnitude of the BRDF and relies on there being little variation in the BRDF shape of

Table 5

Mean absolute surface NBAR differences $\overline{\Delta NBAR}_\lambda$ (Eq. (7)) and mean absolute relative percentage surface NBAR differences $\overline{\Delta NBAR}_\lambda^{\%}$ (Eq. (8)) between the pairs of forward and backward scatter Sentinel-2A surface reflectance values for January (6,600,685 pairs) and April (10,656,197 pairs) in the southern Africa overlapping orbit swaths (locations shown in Fig. 1) normalized to NBAR.

Sentinel-2A band	January		April	
	$\overline{\Delta NBAR}_\lambda$	$\overline{\Delta NBAR}_\lambda^{\%}$	$\overline{\Delta NBAR}_\lambda$	$\overline{\Delta NBAR}_\lambda^{\%}$
2 (blue)	0.0122	16.8068	0.0082	16.5316
3 (green)	0.0109	9.3809	0.0071	8.4644
4 (red)	0.0122	7.6665	0.0088	8.2555
8 (NIR)	0.0151	5.5458	0.0144	5.3160
11 (SWIR)	0.0197	5.3856	0.0128	6.0531
12 (SWIR)	0.0200	6.6386	0.0119	6.7008

Table 6

Summary of the ordinary least squares (OLS) linear regressions of the surface NBAR differences illustrated in Figs. 7 and 8 and for the other Sentinel-2A bands. A total of 6,600,685 (January) and 10,656,197 (April) values were used to derive the OLS regressions where Δ = blue orbit minus red orbit surface NBAR and θ_v = blue orbit view zenith angle (see Fig. 1). The OLS regression coefficient of determination (r^2), the OLS regression F-test p-value, and the B-F difference are shown.

Sentinel-2A band	January			April		
	OLS equation	OLS r^2 (p-value)	B-F difference	OLS equation	OLS r^2 (p-value)	B-F difference
2 (blue)	$\Delta = -0.0008 \theta_v - 0.0001$	0.2432 (<0.0001)	0.0188	$\Delta = 0.0001 \theta_v - 0.0009$	0.0035 (<0.0001)	0.0016
3 (green)	$\Delta = -0.0007 \theta_v + 0.0006$	0.2266 (<0.0001)	0.0166	$\Delta = 0.0000 \theta_v - 0.0005$	0.0020 (<0.0001)	0.0011
4 (red)	$\Delta = -0.0007 \theta_v + 0.0005$	0.1624 (<0.0001)	0.0159	$\Delta = 0.0000 \theta_v - 0.0018$	0.0005 (<0.0001)	0.0007
8 (NIR)	$\Delta = -0.0007 \theta_v + 0.0024$	0.1193 (<0.0001)	0.0178	$\Delta = -0.0002 \theta_v - 0.0006$	0.0080 (<0.0001)	0.0043
11 (SWIR)	$\Delta = -0.0010 \theta_v + 0.0041$	0.1002 (<0.0001)	0.0230	$\Delta = -0.0001 \theta_v - 0.0029$	0.0026 (<0.0001)	0.0024
12 (SWIR)	$\Delta = -0.0012 \theta_v + 0.0024$	0.1605 (<0.0001)	0.0283	$\Delta = -0.0003 \theta_v - 0.0035$	0.0273 (<0.0001)	0.0071

terrestrial surfaces in the near-nadir region. The approach was developed for Landsat NBAR derivation based on observations that BRDF shapes are sufficiently similar over the narrow Landsat field of view that a fixed set of MODIS BRDF spectral model parameters can be used (Roy et al., 2016a). This may not be the case for all land surfaces at the higher view zenith angles observed by Sentinel-2A (20.6° field of view compared to the Landsat 15° field of view). Second, the fixed set of BRDF spectral model parameters, derived from a global year of highest quality snow-free MODIS 500 m BRDF product values (Table 1), may

not provide a sufficient representation of the surface reflectance anisotropy at Landsat or Sentinel-2A scale (Zhang and Roy, 2016). The spatial scale dependency of BRDF is complex and an on-going area of research (Pinty et al., 2002; Román et al., 2011). Third, although the Sentinel-2A and MODIS bands have similar central wavelengths their bandwidths are not the same (Table 1) and it is established that reflectance derived from sensors with different bandwidths is usually different (Steven et al., 2003; Teillet et al., 2007). However, as the c-factor used to adjust the Sentinel-2A reflectance to NBAR is derived as the ratio of MODIS

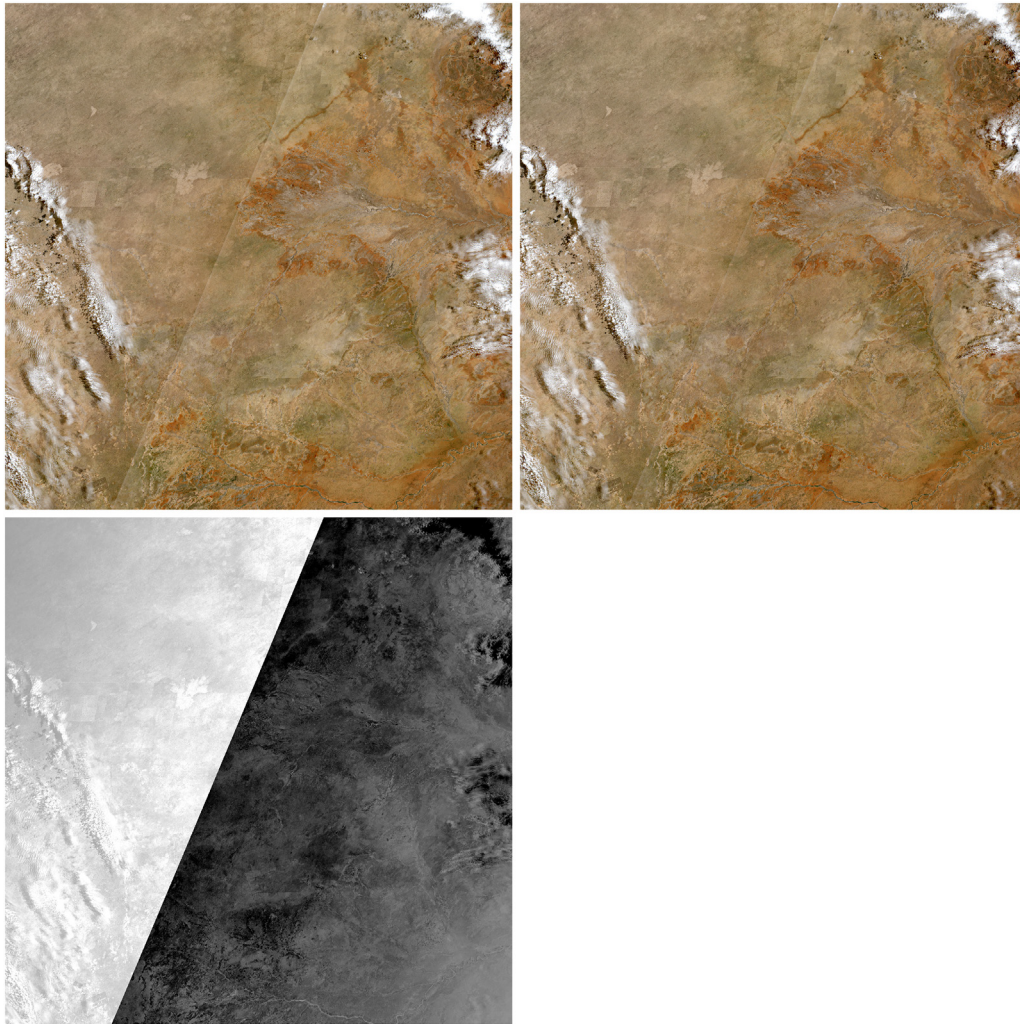


Fig. 9. True color Sentinel-2A *Top Left*: surface reflectance (i.e., before BRDF correction), *Top Right*: surface NBAR (i.e., after BRDF correction), *Bottom Left*: Red surface NBAR – Red surface reflectance (positive values shown by white tones). The data are over a 158×158 km (5295×5295 30 m pixel) global WELD tile encompassing the Botswana and South Africa border (centered at 26.008369°E , 25.000132°S , defined in the MODIS sinusoidal projection) derived from two overlapping Sentinel-2A swaths sensed January 4th, 2016 (western orbit, forward scatter direction) and January 1st, 2016 (eastern orbit, back scatter direction) (i.e., orbits 004 and 001, Fig. 1. left). The true color data (top row) are illustrated with the same red, green and blue display stretch parameters to enable their meaningful visual comparison. (For interpretation of the references to color in this figure legend, the reader is referred to the web version of this article.)

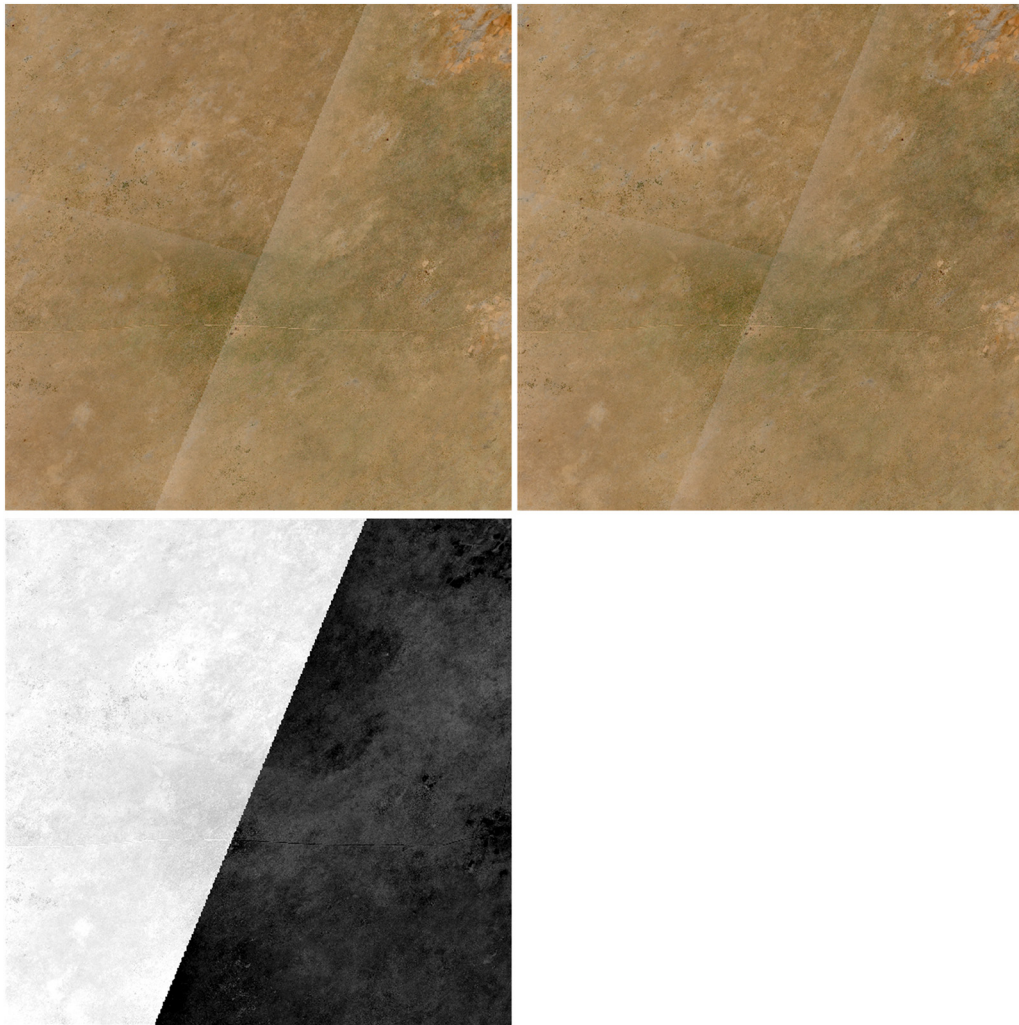


Fig. 10. Detail showing a 18×18 km spatial subset of the Fig. 9 data. The subset is located near the tile (Fig. 9) center and over the western and eastern Sentinel-2A swath boundary (oriented NNE to SSW). The western orbit encompasses an along-track boundary between two Sentinel L1C tiles that is oriented WNW to ESE and evident in the true color data from the subset center to the subset edge.

predicted reflectance for observed and normalized geometry (Eq. (5)) this is less important. Because of the ratio formulation, multiplicative reflectance differences between Sentinel-2 and MODIS spectral reflectance will cancel. Fourth, it is unknown if the Sentinel-2A MSI calibration or SEN2COR atmospheric correction have significant angular dependencies that would affect the study results. The Sentinel-2A MSI has an absolute calibration knowledge uncertainty performance goal of 3% and a specification of 5% (Drusch et al., 2012) which is comparable to the Landsat-8 OLI (Markham et al., 2014). Recent Sentinel-2A calibration validation activities indicate that the 3% goal has been satisfied except for the MSI blue bands (Gascon et al., 2016). The atmospheric correction accuracy of the SEN2COR code is unknown but will be variable and depend on the surface and atmospheric conditions. Qualitative inspection of sample January NBAR data indicate that residual BRDF effects in the NBAR data are comparable in magnitude to residual SEN2COR atmospheric correction errors.

Visually, the Sentinel-2A NBAR images illustrated in this paper, and also evident in publically available global coverage 30 m Landsat 5 and 7 NBAR surface reflectance data sets (<http://globalweld.cr.usgs.gov/collections/>), indicate that the MODIS BRDF spectral parameter c-factor approach provides only a generalized normalization and that certain locations and times may have greater reflectance anisotropy than captured by the BRDF spectral model parameters. This is difficult to unambiguously ascertain from visual inspection of large area NBAR data due to differences among the date of acquisition of the input

satellite data and so the presence of confounding reflectance differences due to changes in the surface and residual atmospheric contamination.

This study did not consider the Sentinel-2A red edge bands (705, 740, 783 nm central wavelengths). This is because there are no MODIS red edge BRDF spectral model parameters available to undertake the Sentinel-2A red-edge band NBAR derivation. MODIS has red edge bands configured with gain settings and signal-to-noise ratios designed for ocean monitoring that are not suitable for land surface monitoring (Esaias et al., 1998). The red edge encompasses the abrupt increase in leaf reflectance from red wavelengths, where leaf reflectance is low due to chlorophyll absorption, to NIR wavelengths where leaf reflectance is high due to leaf internal scattering (Gates et al., 1965; Clevers and Gitelson, 2013). Some form of spectral interpolation between the MODIS red and NIR land band BRDF model parameter values (Table 1) may provide a solution. However, we note that the red and NIR wavelengths have quite different BRDF characteristics; typically red wavelengths have higher relative reflectance variation with respect to view and solar angle than the NIR (Johnson, 1994; Sandmeier and Strahler, 2000; Gao et al., 2002). Further work to investigate the BRDF normalization of the Sentinel-2A red edge bands is recommended.

The quantitative results reported in this paper, i.e., concerning the degree of BRDF effects observed in Sentinel-2A data and the efficacy of the MODIS BRDF spectral parameter c-factor normalization approach applied to Sentinel-2 data, may not be globally representative. Although more than 17 million pairs of forward and back scatter reflectance

observations were extracted across southern Africa they did not include evergreen needleleaf and snow and ice land covers. Moreover, the surface condition, and not just the land cover, may influence the surface BRDF. The reported analyses of two 10-day periods of Sentinel-2 data are unlikely to capture all surface condition changes, for example, changes in the BRDF of deciduous forests under leaf-on and leaf-off conditions. In addition, although observations sensed close to the solar principal and orthogonal planes were considered, observations sensed with solar zenith $> 50^\circ$, where BRDF effects become particularly pronounced, were not considered.

The recent 2017 launch of Sentinel-2B will provide two Sentinel 2 satellites with global observation coverage every 5 days (Drusch et al., 2012). Research to consider the variation in Sentinel-2 solar geometry is needed to determine the appropriate solar zenith angle for global Sentinel-2 NBAR derivation (Zhang et al., 2016). In this study the Sentinel-2A NBAR was derived for a nadir view and setting the solar zenith to the mean of the observed solar zenith angles of the forward or backward scattering pixel observations sensed 3 or 7 days apart. The extrapolation from the observed to the modeled NBAR solar zenith was no more than half the change in solar zenith over the 3 or 7 day separation, no more than 2.1° (January) or 4.8° (April), and was not significant compared to the variation in the view zenith. This may not be the case for other latitudes and times of year.

The future availability of several Sentinel-2 and Landsat satellites may provide sufficient cloud-free observations to enable reliable local parameterization of the surface reflectance anisotropy over Sentinel-2 observation conditions. This may preclude the need for the MODIS BRDF spectral parameter c-factor normalization approach to derive Sentinel-2A NBAR. Future work to investigate this and the challenges in harmonizing the different sensor data, including the solar zenith variation among sensors, for this purpose are recommended.

Acknowledgements

This research was funded by the NASA Land Cover/Land Use Change (LCLUC14-2): Multi-Source Land Imaging Science Program, Grant NNX15AK94G and by the U.S. Department of Interior, U.S. Geological Survey (USGS), Grant G12PC00069. The European Space Agency project management and staff are thanked for provision of the Sentinel-2A data.

References

- Archibald, S., Scholes, R.J., Roy, D.P., Roberts, G., Boschetti, L., 2010. Southern African fire regimes as revealed by remote sensing. *Int. J. Wildland Fire* 19, 861–878.
- Barnes, W.L., Pagano, T.S., Salomonson, V.V., 1998. Prelaunch characteristics of the moderate resolution imaging spectroradiometer (MODIS) on EOS-AM1. *IEEE Trans. Geosci. Remote Sens.* 36 (4), 1088–1100.
- Chopping, M.J., 2000. Large-scale BRDF retrieval over New Mexico with a multiangular NOAA AVHRR dataset. *Remote Sens. Environ.* 74 (1), 163–191.
- Claverie, M., Vermote, E.F., Franch, B., Masek, J.G., 2015. Evaluation of the Landsat-5 TM and Landsat-7 ETM+ surface reflectance products. *Remote Sens. Environ.* 169, 390–403.
- Clevers, J.G., Gitelson, A.A., 2013. Remote estimation of crop and grass chlorophyll and nitrogen content using red-edge bands on Sentinel-2 and -3. *Int. J. Appl. Earth Obs. Geoinf.* 23, 344–351.
- Drusch, M., Del Bello, U., Carlier, S., Colin, O., Fernandez, V., Gascon, F., Hoersch, B., Isola, C., Laberinti, P., Martimort, P., 2012. Sentinel-2: ESA's optical high-resolution mission for GMES operational services. *Remote Sens. Environ.* 120, 25–36.
- ESA (European Space Agency), 2015. Sentinel-2 User Handbook, Issue 1, Revision 2, 24/07/2015. ESA Standard Document.
- Esaia, W.E., Abbott, M.R., Barton, I., Brown, O.B., Campbell, J.W., Carder, K.L., Clark, D.K., Evans, R.H., Hoge, F.E., Gordon, H.R., Balch, W.M., Balch, W.M., 1998. An overview of MODIS capabilities for ocean science observations. *IEEE Trans. Geosci. Remote Sens.* 36 (4), 1250–1265.
- Flood, N., Danaher, T., Gill, T., Gillingham, S., 2013. An operational scheme for deriving standardised surface reflectance from Landsat TM/ETM+ and SPOT HRG imagery for Eastern Australia. *Remote Sens.* 5 (1), 83–109.
- Franch, B., Vermote, E.F., Sobrino, J.A., Fédèle, E., 2013. Analysis of directional effects on atmospheric correction. *Remote Sens. Environ.* 128, 276–288.
- Friedl, M.A., Sulla-Menashe, D., Tan, B., Schneider, A., Ramankutty, N., Sibley, A., Huang, X., 2010. MODIS collection 5 global land cover: algorithm refinements and characterization of new datasets. *Remote Sens. Environ.* 114, 168–182.
- Gao, F., Jin, Y., Schaaf, C.B., Strahler, A.H., 2002. Bidirectional NDVI and atmospherically resistant BRDF inversion for vegetation canopy. *IEEE Trans. Geosci. Remote Sens.* 40 (6), 1269–1278.
- Gao, F., He, T., Masek, J.G., Shuai, Y., Schaaf, C.B., Wang, Z., 2014. Angular effects and correction for medium resolution sensors to support crop monitoring. *IEEE J. Sel. Top. Appl. Earth Obs. Remote Sens.* 7 (11), 4480–4489.
- Gascon, F., Thépaut, O., Jung, M., Francesconi, B., Louis, J., Lonjou, V., Lafrance, B., Massera, S., Gaudel-Vacaresse, A., Languille, F., Alhamoud, B., Viallefont, F., Bieniarz, J., Pflug, B., Clerc, S., Pessiot, L., Trémas, T., Cadau, E., De Bonis, R., Isola, C., Martimort, P., Fernandez, V., 2016. Copernicus Sentinel-2 Calibration and Products Validation Status. 2016:p. 2016100078. <http://dx.doi.org/10.20944/preprints201610.0078.v1> (Preprints).
- Gates, D.M., Keegan, H.J., Schleter, J.C., Weidner, V.R., 1965. Spectral properties of plants. *Appl. Opt.* 4 (1), 11–20.
- Hapke, B., DiMucci, D., Nelson, R., Smythe, W., 1996. The cause of the hot spot in vegetation canopies and soils: shadow-hiding versus coherent backscatter. *Remote Sens. Environ.* 58 (1), 63–68.
- Hauteceur, O., Leroy, M.M., 1998. Surface bidirectional reflectance distribution function observed at global scale by POLDER/ADEOS. *Geophys. Res. Lett.* 25 (22), 4197–4200.
- Hu, B., Lucht, W., Strahler, A.H., 1999. The interrelationship of atmospheric correction of reflectances and surface BRDF retrieval: a sensitivity study. *IEEE Trans. Geosci. Remote Sens.* 37 (2), 724–738.
- Huang, H., Roy, D.P., Boschetti, B., Zhang, H.K., Yan, L., Kumar, S.S., Gomez-Dans, J., Li, J., 2016. Separability analysis of Sentinel-2A multi-spectral instrument (MSI) data for burned area discrimination. *Remote Sens.* 8 (10), 873.
- Irons, J.R., Dwyer, J.L., Barsi, J.A., 2012. The next Landsat satellite: the Landsat data continuity mission. *Remote Sens. Environ.* 122, 11–21.
- Johnson, L.F., 1994. Multiple view zenith angle observations of reflectance from ponderosa pine stands. *Int. J. Remote Sens.* 15, 3859–3865.
- Ju, J., Roy, D.P., Vermote, E., Masek, J., Kovalsky, V., 2012. Continental-scale validation of MODIS-based and LEDAPS Landsat ETM+ atmospheric correction methods. *Remote Sens. Environ.* 122, 175–184.
- Kaufman, Y.J., Sendra, C., 1988. Algorithm for automatic atmospheric corrections to visible and near-IR satellite imagery. *Int. J. Remote Sens.* 9 (8), 1357–1381.
- Kimes, D.S., 1983. Dynamics of directional reflectance factor distributions for vegetation canopies. *Appl. Opt.* 22 (9), 1364–1372.
- Languille, F., Déchoz, C., Gaudel, A., Greslou, D., de Lussy, F., Trémas, T., Poulain, V., 2015. Sentinel-2 geometric image quality commissioning: first results. *Proc. SPIE* 2015. <http://dx.doi.org/10.1117/12.2194339>.
- Lee, T.Y., Kaufman, Y.J., 1986. Non-Lambertian effects on remote sensing of surface reflectance and vegetation index. *IEEE Trans. Geosci. Remote Sens.* 24, 699–708.
- Loveland, T.R., Irons, J.R., 2016. Landsat 8: the plans, the reality, and the legacy. *Remote Sens. Environ.* 185, 1–6.
- Markham, B., Barsi, J., Kvaran, G., Ong, L., Kaita, E., Biggar, S., Czaplá-Myers, J., Mishra, N., Helder, D., 2014. Landsat-8 operational land imager radiometric calibration and stability. *Remote Sens.* 6 (12), 12275–12308.
- Müller-Wilm, U., 2016. Sen2Cor Configuration and User Manual, Ref. S2-PDGS-MPC-L2A-SUM-V2.3. Telespazio VEGA Deutschland GmbH: Darmstadt, Germany.
- Pinty, B., Widlowski, J.L., Gobron, N., Verstraete, M.M., Diner, D.J., 2002. Uniqueness of multiangular measurements. I. An indicator of subpixel spectral heterogeneity from MISR. *IEEE Trans. Geosci. Remote Sens.* 40 (7), 1560–1573.
- Rahman, H., 1996. Atmospheric optical depth and water vapour effects on the angular characteristics of surface reflectance in NOAA AVHRR. *Int. J. Remote Sens.* 17 (15), 2981–2999.
- Roberts, G., 2001. A review of the application of BRDF models to infer land cover parameters at regional and global scales. *Prog. Phys. Geogr.* 25, 483–511.
- Román, M.O., Gatebe, C.K., Schaaf, C.B., Poudyal, R., Wang, Z., King, M.D., 2011. Variability in surface BRDF at different spatial scales (30 m – 500 m) over a mixed agricultural landscape as retrieved from airborne and satellite spectral measurements. *Remote Sens. Environ.* 115 (9), 2184–2203.
- Roujean, J.L., Leroy, M., Deschamps, P.Y., 1992. A bidirectional reflectance model of the Earth's surface for the correction of remote sensing data. *J. Geophys. Res. Atmos.* 97 (D18), 20455–20468.
- Roy, D.P., Ju, J., Lewis, P., Schaaf, C., Gao, F., Hansen, M., Lindquist, E., 2008. Multi-temporal MODIS–Landsat data fusion for relative radiometric normalization, gap filling, and prediction of Landsat data. *Remote Sens. Environ.* 112 (6), 3112–3130.
- Roy, D.P., Qin, Y., Kovalsky, V., Vermote, E.F., Ju, J., Egorov, A., Hansen, M.C., Kommareddy, I., Yan, L., 2014. Continuous United States demonstration and characterization of MODIS-based Landsat ETM+ atmospheric correction. *Remote Sens. Environ.* 140, 433–449.
- Roy, D.P., Zhang, H.K., Ju, J., Gomez-Dans, J.L., Lewis, P.E., Schaaf, C.B., Sun, Q., Li, J., Huang, H., Kovalsky, V., 2016a. A general method to normalize Landsat reflectance data to nadir BRDF adjusted reflectance. *Remote Sens. Environ.* 176, 255–271.
- Roy, D.P., Li, J., Zhang, H.K., Yan, L., 2016b. Best practices for the reprojection and resampling of Sentinel-2 multi spectral instrument level 1C data. *Remote Sens. Lett.* 7 (11), 1023–1032.
- Sandmeier, S.S., Strahler, A.H., 2000. BRDF laboratory measurements. *Remote Sens. Rev.* 18 (2–4), 481–502.
- Sandmeier, S., Müller, C., Hosgood, B., Andreoli, G., 1998. Physical mechanisms in hyperspectral BRDF data of grass and watercress. *Remote Sens. Environ.* 66 (2), 222–233.
- Schaaf, C., Gao, F., Strahler, A., Lucht, W., Li, X., Tsang, T., Strugnell, N., Zhang, X., Jin, Y., Muller, J.-P., Lewis, P., Barnsley, M., Hobson, P., Disney, M., Roberts, G., Dunderdale, M., d'Entremont, R., Hu, B., Liang, S., Privette, J., Roy, D., 2002. First operational BRDF, albedo and nadir reflectance products from MODIS. *Remote Sens. Environ.* 83, 135–148.
- Steven, M.D., Malthus, T.J., Baret, F., Xu, H., Chopping, M.J., 2003. Intercalibration of vegetation indices from different sensor systems. *Remote Sens. Environ.* 88 (4), 412–422.

- Swap, R.J., Annegarn, H.J., Suttles, J.T., Haywood, J., Helmlinger, M.C., Hely, C., Hobbs, P.V., Holben, B.N., Ji, J., King, M., Landmann, T., Maenhaut, W., Otter, L., Pak, B., Piketh, S.J., Platnick, S., Privette, J., Roy, D., Thompson, A.M., Ward, & D., Yokelson, R., 2002. The Southern African Regional Science Initiative (SAFARI 2000): overview of the dry-season field campaign. *S. Afr. J. Sci.* 98, 125–130.
- Tanre, D., Herman, M., Deschamps, P.Y., 1981. Influence of the background contribution upon space measurements of ground reflectance. *Appl. Opt.* 20 (20), 3676–3684.
- Teillet, P.M., Fedosejevs, G., Thome, K.J., Barker, J.L., 2007. Impacts of spectral band difference effects on radiometric cross-calibration between satellite sensors in the solar-reflective spectral domain. *Remote Sens. Environ.* 110 (3), 393–409.
- Wolfe, R.E., Roy, D.P., Vermote, E., 1998. MODIS land data storage, gridding, and compositing methodology: level 2 grid. *IEEE Trans. Geosci. Remote Sens.* 36 (4), 1324–1338.
- Yan, L., Roy, D.P., Zhang, H.K., Li, J., Huang, H., 2016. An automated approach for sub-pixel registration of Landsat-8 operational land imager (OLI) and Sentinel-2 multi spectral instrument (MSI) imagery. *Remote Sens.* 8 (6), 520.
- Zhang, H.K., Roy, D.P., 2016. Landsat 5 Thematic Mapper reflectance and NDVI 27-year time series inconsistencies due to satellite orbit change. *Remote Sens. Environ.* 186, 217–233.
- Zhang, H.K., Roy, D.P., Kovalsky, V., 2016. Optimal solar geometry definition for global long term Landsat time series bi-directional reflectance normalization. *IEEE Trans. Geosci. Remote Sens.* 54 (3), 1410–1418.